

# Predicting Discharge from a Complex Karst System Using the Ensemble Smoother with Multiple Data Assimilation

Alessandro Pansa<sup>1</sup>, Ilaria Butera<sup>2</sup>, J. Jaime Gómez-Hernández<sup>3</sup>, and Bartolomeo Vigna<sup>4</sup>

<sup>1</sup>Interateneo Department of Land Science, Planning and Policy, University of Turin, Italy. Email: alessandro.pansa@unito.it

<sup>2</sup>Department of Environment, Land and Infrastructure Engineering, Politecnico di Torino. Italy. Email: ilaria.butera@polito.it

<sup>3</sup>Institute for Water and Environmental Engineering. Universitat Politècnica de València. Spain. Email: jgomez@upv.es

<sup>4</sup>Department of Environment, Land and Infrastructure Engineering, Politecnico di Torino. Italy. Email: bartolomeo.vigna@polito.it

## Abstract

Can the ensemble smoother with multiple data assimilation be used to predict discharge in an Alpine karst aquifer? The answer is yes, at least, for the Bossea aquifer studied. The ensemble smoother is used to fit a unit hydrograph simultaneously with other parameters in a hydrologic model, such as base flow, infiltration coefficient, or snow melting contribution. The fitting uses observed discharge flow rates, daily precipitations, and temperatures to define the model's parameters. The data assimilation approach gives excellent results for fitting individual events. After the analysis of 27 such events, two average models are defined to be used to predict flow discharge from precipitation and temperature, one model for prediction during spring (when snow melting has an impact) and another one during autumn, yielding acceptable results, particularly for the fall rainfall events. The lesser performance for the spring events may indicate that the snow melting approximation needs to be revised. The results also show that the parameterization of the infiltration

24 coefficient needs further exploration. Overall, the main conclusion is that the ensemble smoother  
25 could be used to define a characteristic “signature” of a karst aquifer to be used in forecast analyses.  
26 The reasons for using the ensemble smoother instead of other stochastic approaches are that it is  
27 easy to use and explain and provides an estimation of the uncertainty about the predictions.

## 28 1 INTRODUCTION

29 A quarter of the world population depends, partially or totally, on karst aquifers (Hartmann  
30 et al. 2015). Their importance is unquestionable, and many efforts have been made to understand  
31 their behavior and model them. One such effort is the vulnerability analysis done by (Banzato  
32 et al. 2017) using the VESPA method. But karst aquifers are very complex, and modeling their  
33 behavior is quite difficult (White 2003). One approach that has not been sufficiently explored in the  
34 study of karst aquifers is data assimilation algorithms. These algorithms have been successfully  
35 applied to solve environmental problems such as reverse flow routing identification (Todaro et al.  
36 2019), hydrological problems (Khaki et al. 2020; Sun et al. 2020; Shokri et al. 2018; Bauser et al.  
37 2018), contaminant source identification (Butera et al. 2021; Xu and Gómez-Hernández 2016;  
38 Chen et al. 2021; Gómez-Hernández and Xu 2022) or basin model building (Li et al. 2015). In  
39 this work, we studied the application of the ensemble smoother with multiple data assimilation  
40 (ES-MDA) to build a hydrological model for flow rate prediction in a karst aquifer using the well-  
41 known instantaneous unit hydrograph method (Sherman 1932) and the rational formula (Kuichling  
42 1889), with the necessary adaptations to the specifics of the case study. The aquifer studied is the  
43 Bossea-Artesinera karst aquifer, located in northwest Italy, in the Maritime Alps (Civita et al. 1990).

44 To the best of the author’s knowledge, the ensemble smoother has not been applied before in  
45 the hydrological modeling of a karst aquifer. Some of the challenges that have been addressed in  
46 the present work include the modeling of infiltration as a time-varying infiltration coefficient, the  
47 classification of precipitation into snowfall and rainfall, and the transformation of snow into water  
48 equivalent infiltration (this problem is well known, and many studies pointed out the relevance of  
49 the phenomenon in alpine karst aquifers, such as those by Lucianetti et al. (2020) or Jódar et al.  
50 (2020), but still, it remains an open issue (Oaida et al. 2019; Barnett et al. 2005)). The snow water-

51 equivalent calculation follows an approach similar to the one in the Soil and Water Assessment Tool  
52 ([Gassman et al. 2007](#); [Uwamahoro et al. 2021](#)), with a temperature-based identification of snowfall  
53 events and then an estimation of snow water equivalent infiltration during the melting period.

54 It is important to point out that the main objective of the paper is the stochastic analysis of flow  
55 discharges in a karst aquifer using real data. Many of the above-referenced works have demonstrated  
56 data assimilation approaches in synthetic datasets with few applications to real cases. In light of  
57 the successful applications in other environmental problems, this paper pretends to demonstrate  
58 that the ensemble smoother with multiple data assimilation can be applied for karst aquifer analyses  
59 providing meaningful predictions with associated uncertainty. As a secondary objective, this paper  
60 also builds a hydrological model —as complex as the limited available data allows— to relate  
61 precipitation, temperature, and discharge.

62 The ensemble smoother (ES) was introduced by [Van Leeuwen and Evensen \(1996\)](#) to solve  
63 inverse problems as an alternative to the ensemble Kalman filter (EnKF) with augmented state  
64 ([Evensen 1994](#)). Its main advantage is the assimilation of all observation data from all times at  
65 once, yielding more accurate estimates more efficiently than the EnKF, provided that the transfer  
66 function relating observation and model parameters is linear ([Evensen 2003](#)). For non-linear  
67 transfer functions, [Emerick and Reynolds \(2013\)](#) proposed the ensemble smoother with multiple  
68 data assimilation, which uses an iterative approach to assimilate the same data set multiple times,  
69 circumventing the problems related to non-linearities. A good description and comparison of  
70 several ensemble smoother methods can be found in [Evensen \(2018\)](#).

71 The paper is organized as follows: after the introduction, the ensemble smoother and the hydro-  
72 logical model are described; next, the case study is presented, and finally, results and discussions  
73 close the paper.

## 74 **2 METHODS**

### 75 **2.1 Ensemble smoother with multiple data assimilation**

76 The ensemble smoother with multiple data assimilation (ES-MDA) will be used in the context  
77 of inverse modeling to infer the parameters of a hydrological model from time observations of

78 the state variables and forcing terms. The hydrological model is referred to as the system state  
79 transition equation or forward model in the data assimilation literature. In the context of the current  
80 paper, the forward model is a hydrological one that predicts discharge flow in a karstic aquifer from  
81 precipitation and temperature. The model is based on Sherman’s instantaneous unit hydrograph  
82 (IUH) (Sherman 1932). The parameters describing the hydrological model are those defining the  
83 IUH plus the infiltration coefficient plus the parameters defining the snow water equivalent model  
84 needed to convert snow into infiltration. The forcing terms are precipitation and temperature, and  
85 the state variable is the time-varying flow discharge at the outlet. The state transition model is  
86 described in detail in the next section; for now and to describe the ES-MDA, it will be represented  
87 by the function  $g$  dependent on a vector of  $n$  model parameters  $x \in \mathfrak{X}^n$ . If the model parameters  
88 are known, the system state can be calculated as

$$89 \quad y = g(x), \quad (1)$$

90 where  $y \in \mathfrak{X}^m$  is a vector of predicted states uniquely determined by relation (1).

91 The purpose of the ES-MDA is to get an estimate of the parameter vector  $x$  from a set of  
92 observations

$$93 \quad d = H \cdot g(x) + \epsilon, \quad (2)$$

94 where  $d \in \mathfrak{X}^p$  is the subset of the system states that have been observed with some observation  
95 error  $\epsilon$  (the error is assumed Gaussian distributed and with covariance  $R$ ). The dimension of  $d$   
96 does not have to coincide with that of  $y$ , that is, not all states need to be observed; matrix  $H$  is an  
97 observation matrix, generally composed of 0s and 1s, that extracts the subset of states that has been  
98 observed from the entire state vector  $y$  predicted by the forward model. In the hydrological model  
99 used in this manuscript, since the model predicts discharge at a single point—the outlet where it  
100 is observed—the dimensions of  $d$  and  $y$  are the same and equal to the number of time steps  $N_t$  at  
101 which flows are predicted/observed, (therefore,  $H$  is the identity matrix).

102 Estimating state parameters  $x$  proceeds in three steps: initialization, forecast, and update, of  
 103 which the last two are iterated. This iteration is what gives the name of multiple data assimilation  
 104 to the algorithm since each iteration amounts to re-assimilate all observations again to improve the  
 105 last estimate of the parameters.

106 In the initialization process, an ensemble ( $X^0 = [x_1, \dots, x_{N_e}]$ ) of parameter vectors needs to  
 107 be generated, its dimension being  $\mathfrak{R}^{n \times N_e}$ , with  $N_e$  being the number of ensemble members. All  
 108 available prior information can and should be used in this procedure; the closer the initial values  
 109 of the ensemble are to the real parameters, the better. Occasionally, there is little or no prior  
 110 information, and the initial ensemble is generated from non-informative (uniform) distributions  
 111 bounded between minimum and maximum values.

112 In the forecast step, the forward model (1) is used with each member of the ensemble of  
 113 parameters  $X$  to generate an ensemble of predicted states  $Y = [y_1 = g(x_1), \dots, y_{N_e} = g(x_{N_e})]$ ,  
 114  $Y \in \mathfrak{R}^{m \times N_e}$ . The discrepancy between predictions and observations is used in the updating step.

115 The updating step—also known as the assimilation step since it is the step in which observations  
 116 are brought in to improve the parameter estimates—uses the auto-covariance of the states  $C_{YY}$  and  
 117 the cross-covariance between state and parameters  $C_{XY}$ . These covariances are estimated from the  
 118 ensembles of parameters and state predictions by

$$119 \quad C_{XY} = \frac{1}{N_e - 1} (X - \bar{X})(Y - \bar{Y})^T, \quad (3)$$

$$120 \quad C_{YY} = \frac{1}{N_e - 1} (Y - \bar{Y})(Y - \bar{Y})^T, \quad (4)$$

121 where the overbar indicates ensemble mean. At the updating step, the number of multiple assim-  
 122 ilations must have been already decided since they affect the updating equation as explained by  
 123 **Emerick and Reynolds (2013)**; let the number of assimilations be  $N_c$ . The update equation is

$$124 \quad x_{j,i+1} = x_{j,i} + C_{XY}(C_{YY} + \alpha_i R)^{-1} \cdot (d + \sqrt{\alpha_i} \epsilon_j - y_j), \quad (5)$$

125 where  $j$  refers to the ensemble member and  $i$  refers to the assimilation step. After each assimilation,  
 126 a new estimate of the parameters is obtained. The term  $C_{XY}(C_{YY} + \alpha_i R)^{-1}$  is known as the Kalman  
 127 gain. Parameter  $\alpha_i$  is related to the number of assimilations and must satisfy the condition

$$128 \quad \sum_{i=1}^{N_c} \frac{1}{\alpha_i} = 1. \quad (6)$$

129 A simple, commonly used solution is adopting  $\alpha_i = N_c$ . Different authors have proposed other  
 130 methods, such as Evensen (2018) and Emerick (2019). The approach suggested by Rafiee and  
 131 Reynolds (2017) has been used in this work.

132 **The inbreeding problem.** Inbreeding occurs when the filter collapses, that is, all ensemble  
 133 members converge into a single realization with no variability among ensemble members. The  
 134 topic is well known and has been discussed in the literature (Chen et al. 2021; Xu et al. 2013;  
 135 Liang et al. 2012). The main reason behind inbreeding is a poor estimation of  $C_{YY}$  and  $C_{XY}$  by the  
 136 experimental covariances given by (3) and (4).

137 This work has used two main approaches to avoid the inbreeding problem. The first one is the  
 138 use of a damping factor, a number  $\beta$  between 0 and 1 that multiplies the gain in the update step as  
 139 follows

$$140 \quad x_{j,i+1} = x_{j,i} + \beta \cdot C_{XY}(C_{YY} + \alpha_i R)^{-1} \cdot (d + \sqrt{\alpha_i} \epsilon_j - y_j). \quad (7)$$

141 The second one is to apply covariance inflation. Among the alternative covariance inflation  
 142 methods discussed in the literature (Bauser et al. 2018; Anderson 2007; Wang and Bishop 2003),  
 143 the one proposed by Anderson and Anderson (1999) has been chosen after some tests. The selected  
 144 method uses a coefficient  $\lambda$  greater than one —to be chosen by trial and error— to spread the  
 145 updated parameter values around their mean value, effectively increasing their variance. After each  
 146 updating step (7), the parameter values are modified according to

$$147 \quad \dot{X}_j = \lambda \cdot (X_j - \bar{X}_j) + \bar{X}_j \quad (8)$$

148 where the overbar refers to the mean value and the dot to the modified update.

## 149 2.2 Hydrological Model

150 The hydrological model is based on the convolution of an instantaneous unit hydrograph with the  
151 inflow calculated using a modified rational formula (Kuichling 1889) to account for snow melting.  
152 In addition, an initial base flow  $Q_b$  is also considered. Many authors highlighted the importance  
153 of the snowmelt contribution to aquifer recharge, such as Lucianetti et al. (2020) and Jódar et al.  
154 (2020), whose studies dealt with karst systems in alpine and pre-alpine areas. Bittner et al. (2021)  
155 also highlights the influence that the uncertainty associated with snowmelt models exerts on the  
156 modeled discharge. However, in this work, in the absence of distributed data measurements, snow  
157 melting is an unknown to be estimated by the model, driven by simple empirical relationships as  
158 described next. Trying to use a more sophisticated model does not make sense, and, besides, it is  
159 not the main focus of the paper.

160 The equation for the rational method is

$$161 \quad I(t) = \chi(t) \cdot A \cdot (i(t) + Sn(t)), \quad (9)$$

162 where  $I(t)$  [ $L^3T^{-1}$ ] is the total infiltration into the aquifer  $\chi(t)$  [-] is a time-varying infiltration  
163 coefficient,  $A$  [ $L^2$ ] is the recharge area,  $i(t)$  [ $LT^{-1}$ ] is the observed rainfall and  $Sn(t)$  [ $LT^{-1}$ ] is the  
164 snowmelt contribution.

165 Computing the snowmelt contribution to infiltration faces two challenges. First, there is a need  
166 to know whether the precipitation registered at the gauge (a heated gauge) corresponds to snow or  
167 rain. Second, snow accumulates and slowly releases when the temperature is above freezing.

168 After several trial-and-error runs, the following logical expression was derived to classify  
169 precipitation into snow or rain

$$170 \quad snow = (T_{min}^{mm} \leq -1 \vee T_{avg} \leq 1 \vee T_{avg}^{mm} \leq 0 \vee T_{max} \leq 4 \vee T_{min} \leq 1.5) \wedge \\ \wedge (T_{min} \leq 0 \vee T_{min}^{mm} \leq -1), \quad (10)$$

171 where all values are in Celsius degrees,  $T_{min}$  is the minimum daily temperature,  $T_{avg}$  is the average  
 172 daily temperature,  $T_{max}$  is the maximum daily temperature, and  $T_{min}^{mm}$  and  $T_{avg}^{mm}$  are the minimum and  
 173 average values of the temperature moving average over three days; when this expression is true, the  
 174 precipitation fallen is snow.

175 To calculate the snow water equivalent infiltration, a release function of time is constructed that  
 176 takes into account the total precedent fallen snow according to the following expressions

$$177 \quad Sn'(t) = \frac{\Sigma_s}{2\sqrt{2\pi b_1^2}} \cdot e^{-\frac{(t-a_1)^2}{2b_1^2}} + \frac{\Sigma_s}{2\sqrt{2\pi b_2^2}} \cdot e^{-\frac{(t-a_2)^2}{2b_2^2}}, \quad (11)$$

$$178 \quad Sn(t) = \frac{Sn'(t)}{\sum_{t=1}^{N_T} Sn'(t)} \cdot V_s, \quad (12)$$

179 where  $\Sigma_s$  [L] is the cumulative snow-equivalent precipitation measured at the gauge and  $a_1, b_1, a_2, b_2$   
 180 are parameters subject to identification during the inversion process; the intermediate values  $Sn'(t)$   
 181 [ $LT^{-1}$ ] are normalized so that the total snow melting (as snow-water equivalent) matches the  
 182 observed value of fallen snow-equivalent precipitation  $V_s$  [L]. The total number of days simulated  
 183 is  $N_T$ . Notice that snow infiltration happens only when snow is on the ground, and the temperature  
 184 is above 0 °C. Fig. 1 shows a typical result of snow water equivalent computed by this approach. In  
 185 dark blue, both the daily snow precipitation and the cumulative precipitation during the first half of  
 186 the year 2012 are shown, and, in light blue, the melted snow (both daily and accumulated) lagging  
 187 in time with the fallen snow but accumulating to the same total by the end of May 2012.

188 The infiltration is routed to the outlet using the following kinematic equation that provides the  
 189 flow discharge

$$190 \quad Q(t) = \int_0^t I(\tau) \cdot h(t-\tau) d\tau, \quad (13)$$

191 where  $Q(t)$  [ $LT^{-3}$ ] is the discharge flow and  $h(t)$  [-] is the instantaneous unit hydrograph (IUH) to  
 192 be subject to identification during the inversion process. The shape of the IUH is parameterized

193 with the following expressions

$$194 \quad h'(t) = \frac{1}{\sqrt{2\pi v_1^2}} \cdot e^{-\frac{(t-m_1)^2}{2v_1^2}} + \frac{1}{v_2} \cdot e^{-\frac{t}{m_2}}, \quad (14)$$

$$195 \quad h(t) = \frac{h'(t)}{\sum_{t=1}^{N_T} h'(t)}, \quad (15)$$

197 where  $v_1, m_1, v_2, m_2$  are parameters to be identified during the inversion process. The intermediate  
 198 values  $h'(t)$  are normalized to ensure that the area under the IUH equals 1.

199 Replacing (9) into (13) and considering that there could be an antecedent base flow due to  
 200 previous rainfall, the final equation that models the routing of the precipitation into discharge is

$$201 \quad Q(t) = Q_b(t) + \int_0^t [\chi(t) \cdot A \cdot (i(t) + Sn(t))] \cdot h(t - \tau) d\tau, \quad (16)$$

202 where  $Q_b [LT^{-3}]$  is the base flow, which will be assumed to decay exponentially as

$$203 \quad Q_b(t) = Q_g(0) \cdot e^{-q_2 \cdot t}, \quad (17)$$

204 where  $Q_g(0)$  is the flow at the gauge at the beginning of the period analyzed and  $q_2 [T^{-1}]$  is a decay  
 205 rate to be identified during the inversion process.

206 The hydrological model is thus established. Its parameters are the four parameters defining  
 207 the snow melting equation, the four parameters defining the unit hydrograph, the decay coefficient  
 208 for the base flow, plus the daily infiltration coefficients. All these parameters will be subject to  
 209 identification during the inversion process by ES-MDA. Since the updating equation (7) does not  
 210 ensure that the updated values will be constrained within specified limits, the ES-MDA is applied  
 211 to some transform of some of the variables: to ensure that the decay rate  $q_2$  is always positive, the  
 212 ES-MDA works with its logarithm, and to ensure that the infiltration coefficients are between 0 and  
 213 1, the following transformation is used

$$\chi'(t) = \frac{1 - \chi(t)}{\chi(t)}. \quad (18)$$

The input data will be temperatures and precipitations, and the output will be flow discharge. An example of the input data and the observed discharge for an event occurring in the spring of 2012 is shown in Fig. 2.

More complex hydrological models could have been considered, including explicitly processes such as evapotranspiration or interception and even distributing the parameters in space; however, there are no data that would justify the construction of such a model. For this reason, the infiltration model depends only on an infiltration coefficient that lumps together all the processes affecting rainfall until it becomes net inflow into the aquifer; and the routing model is based on the unit hydrograph. The snowmelt component had to be modeled aside; our preliminary tests showed that this process could not be lumped into the infiltration coefficient. The final model for the snow-equivalent infiltration was the simplest one possible (depending only on four parameters) and capable of reproducing the dynamics of snow melting at the site.

### 3 CASE STUDY

The system analyzed in this work is the Bossea-Artesinera karst aquifer. It is located in Northwest Italy, in the Maritime Alps district, and it is a rather complex karst system, well studied and described by [Antonellini et al. \(2019\)](#). In Fig. 3, the study area location is shown. Part of the system is accessible through the Bossea Cave. The infiltration basin covers around 6 km<sup>2</sup>, as indicated by [Civita et al. \(1990\)](#), which is the value used in the model. The entrance to the cave opens onto the middle Corsaglia valley, through which the stream of the same name flows. The primitive glacial morphology has almost disappeared due to the intense erosion by the watercourse. This strong erosion has two main causes: a change in the base level of the Tanaro river, of which the Corsaglia is a tributary, and a recent uplift of the entire Alpine sector where the aquifer is located. Towards the west of the basin, the karst absorption areas open up, consisting of valleys dug by the erosion of temporary waterways. An alternation of waterproof quartzites can be identified, replaced

239 by limestone where the water infiltrates to reach the aquifer. Karst soils are partially covered by  
240 insoluble residues on which vegetation grows. Towards Prato Nevoso, the landscape turns into  
241 gentler karst forms with a grassy cover, where there are some absorbent sinkholes.

242 The climate is strongly influenced by the nearby Mediterranean Sea (about 40 km away) with  
243 abundant rainfall in autumn, generally in November, and in spring, typically in May, while the  
244 driest season is summer. The mountainous environment leads to frequent snow falling in the cold  
245 months, especially in the higher part of the basin, which rises to 2382 m.a.s.l. The winter is mainly  
246 characterized by freezing temperatures, especially at night, and snow precipitations. For these  
247 reasons, a second dry season occurs during the winter. Concerning snowfall, a maximum height  
248 of snow during the season can be found between 50 cm and 250 cm, usually recorded in the late  
249 winter period. There is often a remarkable difference in precipitation between the lower and the  
250 higher areas. The snow melting lasts for the entire springtime, starting in March and continuing  
251 until May. It affects first the sunny slopes, usually east and south, and then those in the shade, north  
252 and west, through the whole spring. The mean annual precipitation calculated during 2001-2018  
253 is equal to 1372 mm with a standard deviation of 381 mm, indicative of a large variability across  
254 the years.

255 Data are gathered in two different locations: the Borello weather station, managed by ARPA  
256 Piemonte, where there are an air thermometer and a heated gauge able to measure rainfalls and  
257 snow falling as millimeters of water; and the Bossea Scientific Station inside the cave, managed  
258 by the Italian Alpine Club and Turin Polytechnic, where the outgoing flow rate is measured with  
259 a weir located on the stream crossing the Bossea Cave. The weir is placed after a pool of calm  
260 water more than 100 m long, allowing to take measurements with a precision of  $1 \text{ Ls}^{-1}$ . The data  
261 analyzed cover from 2001 to 2018. In Fig. 3, the aquifer basin, the Borello weather station, and the  
262 cave entrance —where flow rates are measured— are shown.

## 263 **4 RESULTS**

264 Two exercises have been performed. The first one is fitting: given the information of an event  
265 such as that in Fig. 2, can the parameters of the hydrological model be identified by the ES-MDA?

266 With which degree of uncertainty? The second is a forecasting one: once several events have been  
267 fitted, can a unique set of parameters be extracted from the analysis of all fits that could be used to  
268 forecast flow rates given input precipitations and temperatures?

269 At the end of either exercise, there is not a single prediction of the parameter values but an  
270 ensemble of values for each parameter. This ensemble allows retrieving one value as the best  
271 estimate—it could be the mean or the median, for example—and also a measure of uncertainty  
272 given by the spread of values and summarized by, for instance, the standard deviation or a confidence  
273 interval. Such uncertainty about the predictions should not be confused with the expected time  
274 variability of the discharge; instead, it measures the amount of information in the dataset and how  
275 reliable forecasts are.

#### 276 **4.1 Fitting**

277 The ES-MDA was applied first to fit the event observed during the spring of 2012. The input  
278 data is shown in Fig. 2 and is discretized daily. The ES-MDA is run with 15 data assimilations,  
279 that is,  $N_c = 15$ , and with 1000 ensemble members, that is,  $N_e = 1000$ . The hydrologic model  
280 is run with daily frequency. The parameter vector that has to be identified by the ES-MDA is the  
281 following

$$282 \quad x = [m_1, v_1, m_2, v_2, a_1, b_1, a_2, b_2, \chi'_1, \chi'_2, \dots, \chi'_{N_T}, q'_2], \quad (19)$$

283 where  $N_T$  is the duration in days of the event being analyzed, the prime marks indicate that the  
284 ES-MDA is not applied to the parameters themselves but rather to a transformation of them, as  
285 explained earlier. Just as a recall, the first four parameters serve to define the parametric shape of  
286 the IUH, the next four parameters control the snow water equivalent model, the next  $N_T$  parameters  
287 are the daily infiltration coefficient transforms, and the last parameter is the logarithm of the decay  
288 rate of the base flow.

289 The initial ensemble of realizations is generated by drawing, independently, each value from  
290 the following uniform distributions,  $m_1$  and  $m_2$  from  $\mathcal{U}[1, 5]$ ,  $v_1$  and  $v_2$  from  $\mathcal{U}[5, 10]$ ,  $a_1$ ,  $b_1$ ,

291  $a_2, b_2$  from  $\mathcal{U}[5, 10]$ ,  $\xi_i$  from  $\mathcal{U}[0, 1]$  and  $q_2$  from  $\mathcal{U}[0, 0.5]$ . The ranges of the parameters were  
292 chosen based on prior information or by trial and error as good starting points for the assimilation  
293 algorithms. Particularly, the IUH parameters were guided by previously performed tracer tests.  
294 In any case, the algorithm itself updates the parameter values at each assimilation step without  
295 any constraint on the interval over which the parameters may fall; that is, the range of the initial  
296 set of parameters has only a marginal influence on the final solution given by the ES-MDA. After  
297 the drawing, infiltration and decay coefficients are transformed as indicated in subsection 2.2. To  
298 prevent filter inbreeding, a damping factor of 0.38 and a covariance inflation of 1.12 were used  
299 (again, these two parameters were chosen by trial and error).

300 Figure 4 shows the ensemble of initial daily infiltration rates and the ensemble of initial IUHs  
301 built with the values drawn for  $m_1, v_1, m_2, v_2$  from their corresponding distributions. As noted, these  
302 initial values display a wide variability.

303 The results of the inversion for the data in Fig. 2 are shown in Fig. 5 where the one thousand  
304 final IUHs and the one thousand final daily infiltration coefficients are shown. Also, the infiltration  
305 coefficient ensemble average is shown in red. There is little uncertainty about the final IUH, whereas  
306 the uncertainty about the infiltration coefficients is larger, particularly during the spans when there  
307 is little or no infiltration.

308 Next, the performance of the inverted values is analyzed by predicting the discharge flow rates  
309 using these values. Recall that the ES-MDA does not provide a single answer but an ensemble of  
310 answers. When each of these answers is plugged into the hydrological model, and the model is run,  
311 the resulting flow rates compare pretty well with the observed ones, as seen in Fig. 6. This figure  
312 shows, with a dotted line, the observed flow rates, and with a yellow band, the results obtained  
313 with the ensemble of inverted parameters; the red line is the ensemble average. The reproduction is  
314 quite good except for a few spans, probably due to failure in predicting the snow water equivalent.  
315 The figure also shows, for reference, the base flow in green and the computed average snow water  
316 equivalent precipitation.

317 Besides the visual comparison of predictions versus observations, several performance indi-

318 cators have been computed: the Nash-Sutcliffe efficiency coefficient (NSE) (Nash and Sutcliffe  
 319 1970), the percentage of total volume error, the average bias in flow prediction, and the root mean  
 320 square error. The expressions for these indicators are given below.

321 **Nash-Sutcliffe efficiency**

$$322 \quad NSE = \frac{\sum_{t=1}^{N_T} (Q_o(t) - Q_m(t))^2}{\sum_{t=1}^{N_T} (Q_o(t) - \bar{Q}_o)^2} \quad (20)$$

323 where  $Q_o(t)$  are the observed (daily) flow rates,  $Q_m(t)$  are the median values of the ensemble of  
 324 modeled daily flow rates and  $\bar{Q}_o$  is the mean of the measured flow rates. The summation extends  
 325 over all the days modeled,  $N_T$ .

326 **Percentage volume error**

$$327 \quad VolRelErr(\%) = \frac{V_o - V_m}{V_o} \cdot 100 \quad (21)$$

328 where  $V_o$  is the volume computed by integrating the discharge curve of observed flow rates and  $V_m$   
 329 is the volume calculated by integrating the median values of the ensemble of modeled flow rates.

330 **Average bias**

$$331 \quad Bias = \frac{1}{N_T} \sum_{t=1}^{N_T} (Q_m(t) - Q_o(t)) \quad (22)$$

332 **Root mean square error**

$$333 \quad RMSE = \sqrt{\frac{1}{N_T} \sum_{t=1}^{N_T} (Q_m(t) - Q_o(t))^2} \quad (23)$$

334 For this specific case, the resulting values of these indicators can be seen in Table 1.

335 Regarding potential filter inbreeding, the evolution of the ratio between the root mean square  
 336 error (RMSE) and the average ensemble spread (ES) has been computed for the observed and  
 337 predicted values of the spring 2012 event. The RMSE is calculated, for each day, using Eq. (23),  
 338 and the ES is given by

$$ES = \frac{1}{N_T} \sum_{t=1}^{N_T} \sigma_t \quad (24)$$

with  $\sigma_i$  being the standard deviation of the flow model predictions at a given time  $t$ . Figure 7 shows the evolution of both RMSE and RMSE/ES with the number of data assimilations. While the RMSE measures the prediction error, the ES measures the fluctuation of the predictions around the mean prediction. Desirably the ratio RMSE/ES should be around 1, indicating that there is no filter inbreeding. In the spring 2012 event, the RMSE gets as low as  $14 \text{ L s}^{-1}$  after 15 assimilation cycles, but still, it is 3.5 larger than the ES. While the ratio RMSE/ES is larger than 1, its value is not disproportionate. It cannot be considered an indication of filter inbreeding since much of the RMSE value is due to the estimation bias reported in Table 1.

## 4.2 Forecasting

The above fitting procedure was performed for all 27 identified events in the 2001-2018 year span. Their analysis shows some recurrent behavior that points towards a possible aquifer signature, which could be used for forecasting.

The first thing that could be noticed is that the aquifer response is different in the first half of the year (spring) than in the second half (autumn). Therefore, if such a signature exists, it will differ depending on the season.

Next, an average response is extracted from the analysis and then used to forecast a couple of events, one in each season.

Figure 8 shows the average IUHs from the ensemble of realizations resulting after fitting all events happening in spring between 2001 and 2018. All IUHs show similar behavior, except for spring 2011, which shows a bump around day 20. Two alternatives are proposed for a representative IUH for spring events at the Bossea aquifer: (i) to use the IUH obtained with the average value of the parameters  $m_1, v_1, m_2, v_2$ , (solid red line in the figure), or (ii) consider the average of the IUHs in the figure, and then find the best fitting parameters for  $m_1, v_1, m_2, v_2$  to this average IUH (dashed red line in the figure). After some tests trying to forecast individual events, it was found that the

364 second option is the one that works best and is retained.

365 Similarly, Fig. 9 shows the average IUHs from the ensemble of realizations resulting after fitting  
366 all events happening in the summer/fall between 2001 and 2018. The similarity among the IUHs  
367 is larger than for the spring ones. The same two options to obtain a mean representative IUH were  
368 considered, although the difference between the solid red line (IUH with average parameters) and  
369 the dashed red line (IUH fitted to the average of the individual IUHs) is small.

370 As already mentioned, the representative IUH differs depending on the season. The spring hy-  
371 drograph distributes the discharge over a more extended period. In contrast, the autumn hydrograph  
372 is more explosive, with most flow occurring a few days after precipitation falls.

373 Regarding the infiltration coefficients, Fig. 10 shows a statistical summary of the daily infiltration  
374 coefficients over the calendar year obtained during the fitting exercise to all the events: in red, the  
375 mean value, and in blue, the interval given by the average plus-minus one standard deviation.  
376 Overall, the uncertainty about the infiltration coefficient is significant, but some clear trends are  
377 observed; the infiltration coefficient peaks at the beginning of spring and has the lowest values once  
378 fall has started, with a second lower peak in early December. The mean coefficients in the figure  
379 are the ones chosen to forecast.

380 The analysis of the snow melting parameters  $a_1$ ,  $b_1$ ,  $a_2$ ,  $b_2$  does not show any noticeable trend.  
381 The only conclusion drawn is that a Gamma distribution could fit the resulting values. Their median  
382 values have been chosen for the forecast.

383 Finally, the decay coefficient  $q_2$  used to describe the base flow does not show any pattern either,  
384 and its median value is chosen for the forecast.

385 Having selected the representative parameters of a generic hydrological model for the Bossea  
386 aquifer, the forecast of some observed events is performed without any additional fitting or parameter  
387 adjustment. Figures 11 and 12 show the forecast for the spring 2013 event and for the fall 2016  
388 event, respectively. These figures display, as a dashed black line, the observed discharges and, as a  
389 solid red line, the forecast obtained using the representative parameters described above. Also, the  
390 two solid purple lines show the predictions using the infiltration coefficients from the upper and

391 lower curves in Fig. 10. For completeness, both figures also show the base flow in green and the  
392 rainfall and snow equivalent precipitations in dark blue and light blue, respectively.

393 For it being a blind prediction, the results can be considered acceptable, especially for the fall  
394 event. The existence of a “signature” IUH was clearer for the fall events (see Fig. 9) than for the  
395 spring events (see Fig. 8). The NSE and the error in total flow calculation have been computed for  
396 the red and purple lines in Figs. 11 and 12 and are reported in Tables 2 and 3, respectively. The  
397 NSE, as expected, is much better (closer to 1) for the fall event than for the spring event, although  
398 the error in total volume prediction is the opposite.

## 399 **5 DISCUSSION AND CONCLUSIONS**

400 This paper explores the possibility of identifying the parameters describing a hydrological model  
401 for an Alpine karst system using the ensemble smoother with multiple data assimilation (ES-MDA).  
402 For this purpose, a model coupling the rational method with time-varying infiltration coefficients,  
403 the instantaneous unit hydrograph, and a snow water equivalent precipitation calculation has been  
404 built. The method has been tested using data from the Bossea aquifer in Italy. Despite having only  
405 one meteorological station, the simple black-box-type model can provide discharge predictions that  
406 match the observed values at the discharge flow gaging station.

407 The model has demonstrated its ability to route precipitation onto flow discharge when the  
408 parameters describing it are fitted using the input precipitation and temperature, and the output  
409 discharge as known. These results demonstrate, again, the efficiency of the ensemble-based filters  
410 and smoothers for inverse modeling. Some of the advantages of the ES-MDA are that it considers  
411 all data for all times at once and that, being an ensemble-based method, it always provides an  
412 ensemble of final results from which best estimates for the parameters (such as the mean or the  
413 median) and uncertainty bounds (such as the standard deviation or the interquartile range) can be  
414 extracted; also, the ES-MDA is conceptually simple to explain and very fast in its implementation.

415 Although only one such fit is shown in the paper, the fits corresponding to other events are  
416 equally good, with NSE values never below 0.9, in most cases, above 0.95. The conclusion  
417 that could be drawn from this fitting exercise is that, indeed, the ES-MDA can be used to fit a

418 hydrological model of the kind described in this paper.

419 Then, the question remained of whether a single set of parameters could be deduced from the  
420 fitting of the different events that would be representative of the aquifer and could be used for  
421 forecasting purposes. The different events had to be split into two sets since it was clear that the  
422 response of the aquifer was not the same during spring (with substantial amounts of infiltration  
423 coming from snow melting) as during autumn when the observed response was more explosive and  
424 closer to a fast flood. After the splitting, average values were computed from the individual event  
425 fittings, and an average model was formulated for each season.

426 Using these average models for predictions did not work as remarkably as the individually fitted  
427 models. There is a need to analyze further why this happened and ways to improve the results. The  
428 comparison of the spring and fall models results in a better assessment of the fall model, which  
429 may indicate a need to reevaluate the implementation of the snow equivalent calculation since this  
430 is the main difference between the two seasons.

431 Another item that may need reevaluation is the time-varying infiltration coefficients. Initial  
432 investigations using a constant infiltration coefficient did not work, meaning that an accurate  
433 forecast can only be obtained with infiltration coefficients that vary in time. The average model  
434 presented in Fig. 10 shows a clear cyclic trend over the natural year but also displays too much  
435 short-scale variability. There is a need to explore alternative parameterizations for the infiltration  
436 coefficient, maybe accounting for antecedent precipitation.

437 The analysis of Fig. 11 shows that the model forecasts too much flow in response to the March  
438 and April precipitations. The first observed peak discharge may be due to snowmelt and is not fully  
439 captured by the model. Then the final recession curve (starting in June 2013) corresponds to an  
440 aquifer with a larger storage volume than the one implied by the forecasting model.

441 The analysis of Fig. 12 is more favorable, and the observed discharge is almost perfectly  
442 reproduced by the predicted one using the average model.

443 It is necessary to highlight that the area of the infiltration basin is but a rough estimation and  
444 that a better definition of it could yield more reliable results.

445 It is difficult to conclude whether a signature response can be built for the Bossea aquifer. Still,  
446 it is clear that the ES-MDA is a powerful tool to fit individual events, which could be used to better  
447 understand the dynamics of the complex Bossea karst system. An interesting continuation of this  
448 work would be using the ES-MDA to fit a unique hydrological model to all data for all events  
449 simultaneously. Such an approach could identify that elusive unique response that was not fully  
450 characterized in this work.

## 451 **6 ACKNOWLEDGMENTS**

452 The authors would like to thank the Bossea Cave Scientific Laboratory personnel and ARPA  
453 Piemonte for the many years of work spent maintaining the instrumentation, collecting data, and  
454 sharing the data.

## 455 **7 STATEMENTS & DECLARATIONS**

### 456 **7.1 Funding**

457 J. Jaime Gómez-Hernández acknowledges grant PID2019-109131RB-I00 funded by MCIN/AEI/10.13039/501100011033

### 458 **7.2 Competing interests**

459 The authors have no relevant financial or non-financial interests to disclose.

### 460 **7.3 Author contributions**

461 All authors contributed to the study's conception and design. Model construction, model runs,  
462 and preliminary analyses were performed by Alessandro Pansa, who also wrote the first draft of the  
463 manuscript. All authors commented on and edited the several versions until the current one. All  
464 authors read and approved the final manuscript.

### 465 **7.4 Data availability**

466 The data supporting this study's findings are available from the corresponding author upon  
467 reasonable request.

## 468 **References**

469 Anderson, J. L. (2007). “An adaptive covariance inflation error correction algorithm for ensemble  
470 filters.” *Tellus A: Dynamic Meteorology and Oceanography*, 59, 210–224.

471 Anderson, J. L. and Anderson, S. L. (1999). “A monte carlo implementation of the nonlinear  
472 filtering problem to produce ensemble assimilations and forecasts.” *Monthly Weather Review*,  
473 127, 2741–2758.

474 Antonellini, M., Nannoni, A., Vigna, B., and Waele, J. D. (2019). “Structural control on karst water  
475 circulation and speleogenesis in a lithological contact zone: The bossea cave system (western  
476 alps, italy).” *Geomorphology*, 345, 106832.

477 Banzato, C., Butera, I., Revelli, R., and Vigna, B. (2017). “Reliability of the vespa index in  
478 identifying spring vulnerability level.” *Journal of Hydrologic Engineering*, 22(6), 04017008.

479 Barnett, T. P., Adam, J. C., and Lettenmaier, D. P. (2005). “Potential impacts of a warming climate  
480 on water availability in snow-dominated regions.” *Nature*, 438(7066), 303–309.

481 Bauser, H. H., Berg, D., Klein, O., and Roth, K. (2018). “Inflation method for ensemble kalman  
482 filter in soil hydrology.” *Hydrol. Earth Syst. Sci.*, 22, 4921–4934.

483 Bittner, D., Richieri, B., and Chiogna, G. (2021). “Unraveling the time-dependent relevance of input  
484 model uncertainties for a lumped hydrologic model of a pre-alpine karst system.” *Hydrogeology  
485 Journal*, 29(7), 2363–2379.

486 Butera, I., Gómez-Hernández, J. J., and Nicotra, S. (2021). “Contaminant-source detection in a  
487 water distribution system using the ensemble kalman filter.” *Journal of Water Resources Planning  
488 and Management*, 147(7).

489 Chen, Z., Xu, T., Gómez-Hernández, J. J., and Zanini, A. (2021). “Contaminant spill in a sand-  
490 box with non-gaussian conductivities: Simultaneous identification by the restart normal-score  
491 ensemble kalman filter.” *Mathematical Geosciences*, 53(7), 1587–1615.

492 Civita, M., Gregoretti, F., Morisi, A., Olivero, G., Peano, G., Vigna, B., Villavecchia, E., and  
493 Vittone, F. (1990). *Atti della stazione scientifica di della Grotta di Bossea*, Vol. 23. Gruppo  
494 Speleologico Alpi Marittime C.A.I. Cuneo - Dipartimento Georisorse e Territorio del Politecnico  
495 di Torino, Savigliano.

496 Emerick, A. A. (2019). “Analysis of geometric selection of the data-error covariance inflation for  
497 es-mda.” *Journal of Petroleum Science and Engineering*, 182, 106168.

498 Emerick, A. A. and Reynolds, A. C. (2013). “Ensemble smoother with multiple data assimilation.”  
499 *Computers & Geosciences*, 55, 3–15.

500 Evensen, G. (1994). “Sequential data assimilation with a nonlinear quasi-geostrophic model using  
501 monte carlo methods to forecast error statistics.” *JOURNAL OF GEOPHYSICAL RESEARCH*,  
502 99(C5), 10143.

503 Evensen, G. (2003). “The ensemble kalman filter: theoretical formulation and practical implemen-  
504 tation.” *Ocean Dynamics*, 53(4), 343–367.

505 Evensen, G. (2018). “Analysis of iterative ensemble smoothers for solving inverse problems.”  
506 *Computational Geosciences*, 22(3), 885–908.

507 Gassman, P., Reyes, M., Green, C., and Arnold, J. (2007). “Soil and water assessment tool:  
508 Historical development, applications, and future research directions, the.” *Transactions of the*  
509 *ASABE*, 50(4), 1211–1250.

510 Gómez-Hernández, J. J. and Xu, T. (2022). “Contaminant source identification in aquifers: a critical  
511 view.” *Mathematical Geosciences*, 54(2), 437–458.

512 Hartmann, A., Goldscheider, N., Wagener, T., Lange, J., and Weiler, M. (2015). “Karst water  
513 resources in a changing world: Review of hydrological modeling approaches.” *Reviews of*  
514 *Geophysics*, 22(7), 2018–242.

515 Jódar, J., González-Ramón, A., Martos-Rosillo, S., Heredia, J., Herrera, C., Urrutia, J., Caballero,  
516 Y., Zabaleta, A., Antigüedad, I., Custodio, E., and Lambán, L. J. (2020). “Snowmelt as a  
517 determinant factor in the hydrogeological behaviour of high mountain karst aquifers: The garcés  
518 karst system, central pyrenees (spain).” *Science of The Total Environment*, 748, 141363.

519 Khaki, M., Ait-El-Fquih, B., and Hoteit, I. (2020). “Calibrating land hydrological models and en-  
520 hancing their forecasting skills using an ensemble kalman filter with one-step-ahead smoothing.”  
521 *Journal of Hydrology*, 584, 124708.

522 Kuichling, E. (1889). “The relation between the rainfall and the discharge of sewers in populous

523 districts.” *Transactions of ASCE*, 20, 1–56.

524 Li, N., McLaughlin, D., Kinzelbach, W., Li, W., and Dong, X. (2015). “Using an ensemble smoother  
525 to evaluate parameter uncertainty of an integrated hydrological model of yanqi basin.” *Journal*  
526 *of Hydrology*, 529, 146–158.

527 Liang, X., Zheng, X., Zhang, S., Wu, G., Dai, Y., and Li, Y. (2012). “Maximum likelihood esti-  
528 mation of inflation factors on error covariance matrices for ensemble kalman filter assimilation.”  
529 *Quarterly Journal of the Royal Meteorological Society*, 263–273.

530 Lucianetti, G., Penna, D., Mastrorillo, L., and Mazza, R. (2020). “The role of snowmelt on the  
531 spatio-temporal variability of spring recharge in a dolomitic mountain group, italian alps.” *Water*,  
532 12(8), 2256.

533 Nash, J. E. and Sutcliffe, J. V. (1970). “River flow forecasting through conceptual models part i —  
534 a discussion of principles.” *Journal of Hydrology*, 10(3), 282–290.

535 Oaida, C. M., Reager, J. T., Andreadis, K. M., David, C. H., Levoe, S. R., Painter, T. H., Bormann,  
536 K. J., Trangsrud, A. R., Giroto, M., and Famiglietti, J. S. (2019). “A high-resolution data  
537 assimilation framework for snow water equivalent estimation across the western united states  
538 and validation with the airborne snow observatory.” *Journal of Hydrometeorology*, 20(3), 357–  
539 378.

540 Rafiee, J. and Reynolds, A. C. (2017). “Theoretical and efficient practical procedures for the  
541 generation of inflation factors for es-mda.” *Inverse Problems*, 33(11), 115003.

542 Sherman, L. (1932). “Stream flow from rainfall by the unit graph method.” *Engineering News*  
543 *Record*, 501–502.

544 Shokri, A., Walker, J., van Dijk, A., and Pauwels, V. (2018). “Performance of different en-  
545 semble kalman filter structures to assimilate grace terrestrial water storage estimates into a  
546 high-resolution hydrological model: A synthetic study.” *Water Resuorces Research*, 54(11),  
547 8931–8951.

548 Sun, Y., Bao, W., Valk, K., Brauer, C. C., Sumihar, J., and Weerts, A. H. (2020). “Improving forecast  
549 skill of lowland hydrological models using ensemble kalman filter and unscented kalman filter.”

550 *Water Resources Research*, 56(8).

551 Todaro, V., D’Oria, M., Tanda, M. G., and Gómez-Hernández, J. J. (2019). “Ensemble smoother  
552 with multiple data assimilation for reverse flow routing.” *Computers & Geosciences*, 131, 32–40.

553 Uwamahoro, S., Liu, T., Nzabarinda, V., Habumugisha, J. M., Habumugisha, T., Harerimana, B.,  
554 and Bao, A. (2021). “Modifications to snow-melting and flooding processes in the hydrological  
555 model—a case study in issyk-kul, kyrgyzstan.” *Atmosphere*, 12(12), 1580.

556 Van Leeuwen, P. J. and Evensen, G. (1996). “Data assimilation and inverse methods in terms of a  
557 probabilistic formulation.” *Monthly weather review*, 124(12), 2898–2913.

558 Wang, X. and Bishop, C. H. (2003). “A comparison of breeding and ensemble transform kalman  
559 filter ensemble forecast schemes.” *Journal of atmospheric sciences*, 60(9), 1140–1158.

560 White, W. B. (2003). “Conceptual models for carbonate aquifers.” *Speleogenesis*, 50(2), 180–186.

561 Xu, T. and Gómez-Hernández, J. J. (2016). “Joint identification of contaminant source location,  
562 initial release time and initial solute concentration in an aquifer via ensemble kalman filtering.”  
563 *WATER RESOURCES RESEARCH*, 52(8), 6587–6595.

564 Xu, T., Gómez-Hernández, J. J., Zhou, H., and Li, L. (2013). “The power of transient piezometric  
565 head data in inverse modeling: An application of the localized normal-score enkf with covariance  
566 inflation in a heterogenous bimodal hydraulic conductivity field.” *Advances in Water Resources*,  
567 54, 100–118.

568 **List of Tables**

569 1 Performance indicators for the spring 2012 event . . . . . 25

570 2 NSE and volume errors for the forecasted spring 2013 flood event. . . . . 26

571 3 NSE and volume errors for the forecasted fall 2016 flood event. . . . . 27

**Table 1.** Performance indicators for the spring 2012 event

Bias ( $\text{L s}^{-1}$ )	-3.15
RMSE ( $\text{L s}^{-1}$ )	13.86
Mean Absolute Error ( $\text{L s}^{-1}$ )	7.92
NSE	0.97
Error in total discharge volume (%)	-2

**Table 2.** NSE and volume errors for the forecasted spring 2013 flood event.

Spring 2013 forecast	$\chi - std$	$\chi$	$\chi + std$
NSE	0.60	0.72	0.41
Volume error [%]	-27.98	1.84	31.65
Difference between real volume and estimated volume [ $m^3 \cdot 10^3$ ]	998.750	-65.519	-1129.789

**Table 3.** NSE and volume errors for the forecasted fall 2016 flood event.

Fall 2016 forecast	$\chi - std$	$\chi$	$\chi + std$
NSE	0.52	0.86	0.25
Volume error [%]	-45.56	6.29	59.70
Difference between real volume and estimated volume [ $m^3 \cdot 10^3$ ]	741.647	-102.327	-971.771

572  
573  
574  
575  
576  
577  
578  
579  
580  
581  
582  
583  
584  
585  
586  
587

## List of Figures

1	Fallen snow and estimated snow melting. . . . .	29
2	Data collected for the flood event in spring 2012. . . . .	30
3	Map of the study area. . . . .	31
4	Initial ensembles of IUHs and infiltration coefficients. . . . .	32
5	Final IUHs and infiltration coefficients . . . . .	33
6	Predicted discharges. In yellow, the predictions with the 1000 members of the final ensemble of parameters, and in red, the average of these predictions. . . . .	34
7	RMSE (Root Mean Square Error) and ratio RMSE/ES (Ensemble Spread). . . . .	35
8	Mean of the IUHs obtained for the spring events and the overall average response, in red. . . . .	36
9	Mean of the IUHs obtained for the summer/fall events and the overall average response, in red. . . . .	37
10	Yearly values of infiltration . . . . .	38
11	Example of reconstructed event dating back to spring 2013. . . . .	39
12	Example of reconstructed event dating back to spring 2016. . . . .	40

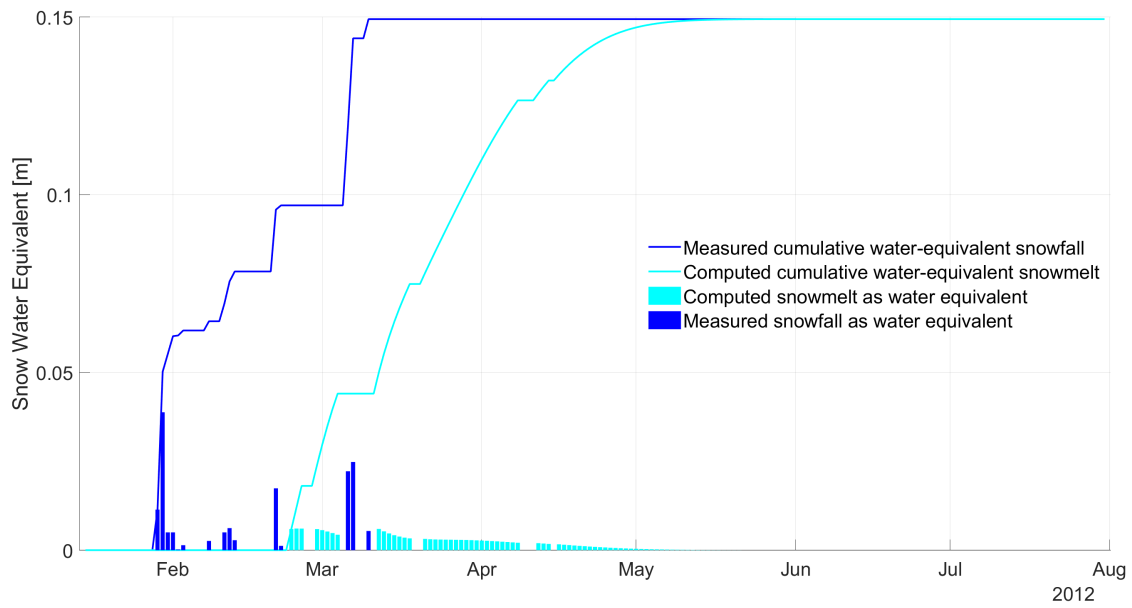


**Figure 1.** Fallen snow (dark blue) and estimated snow melting (light blue).

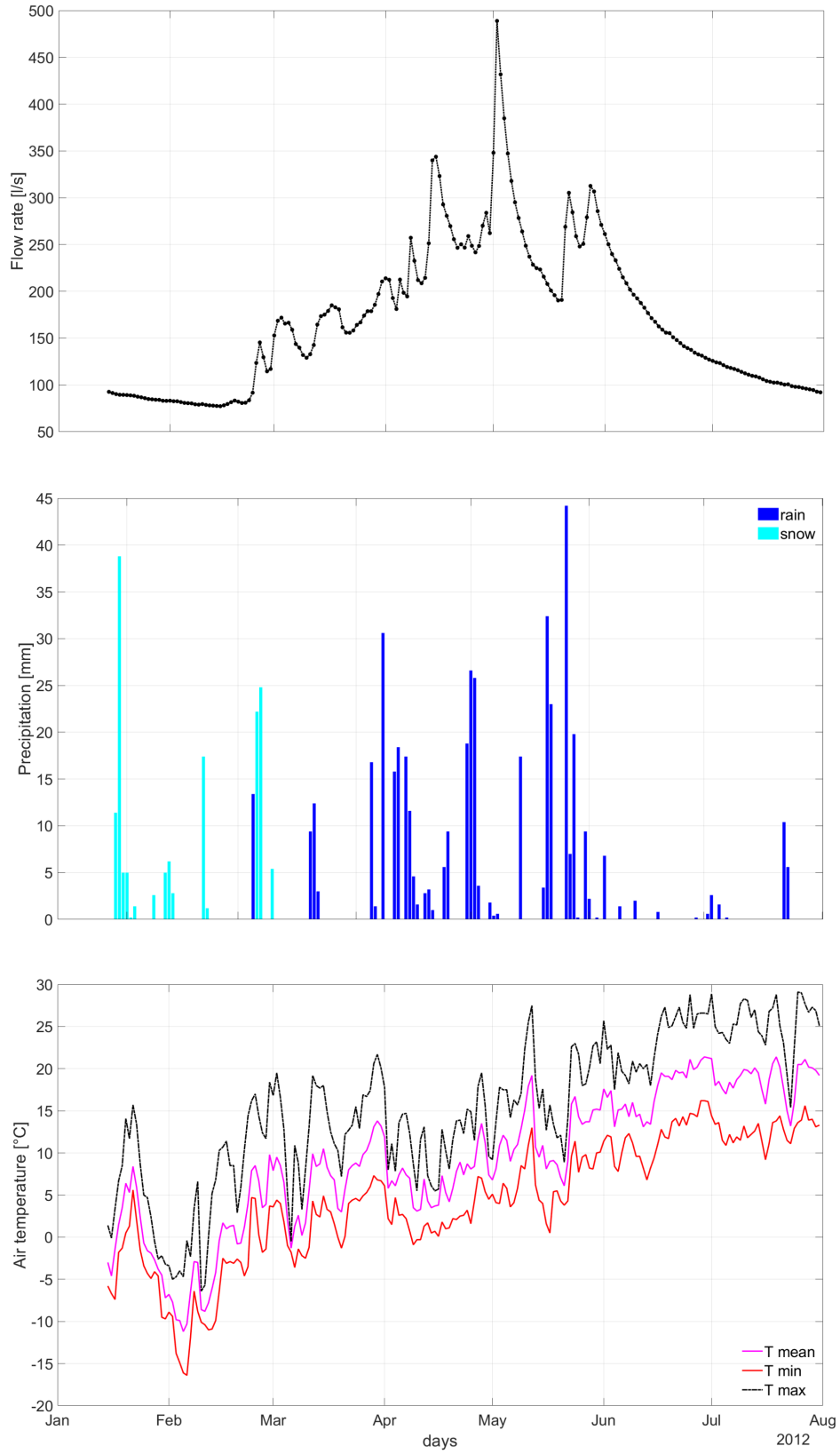


**Figure 2.** Data collected for the flood event in spring 2012.

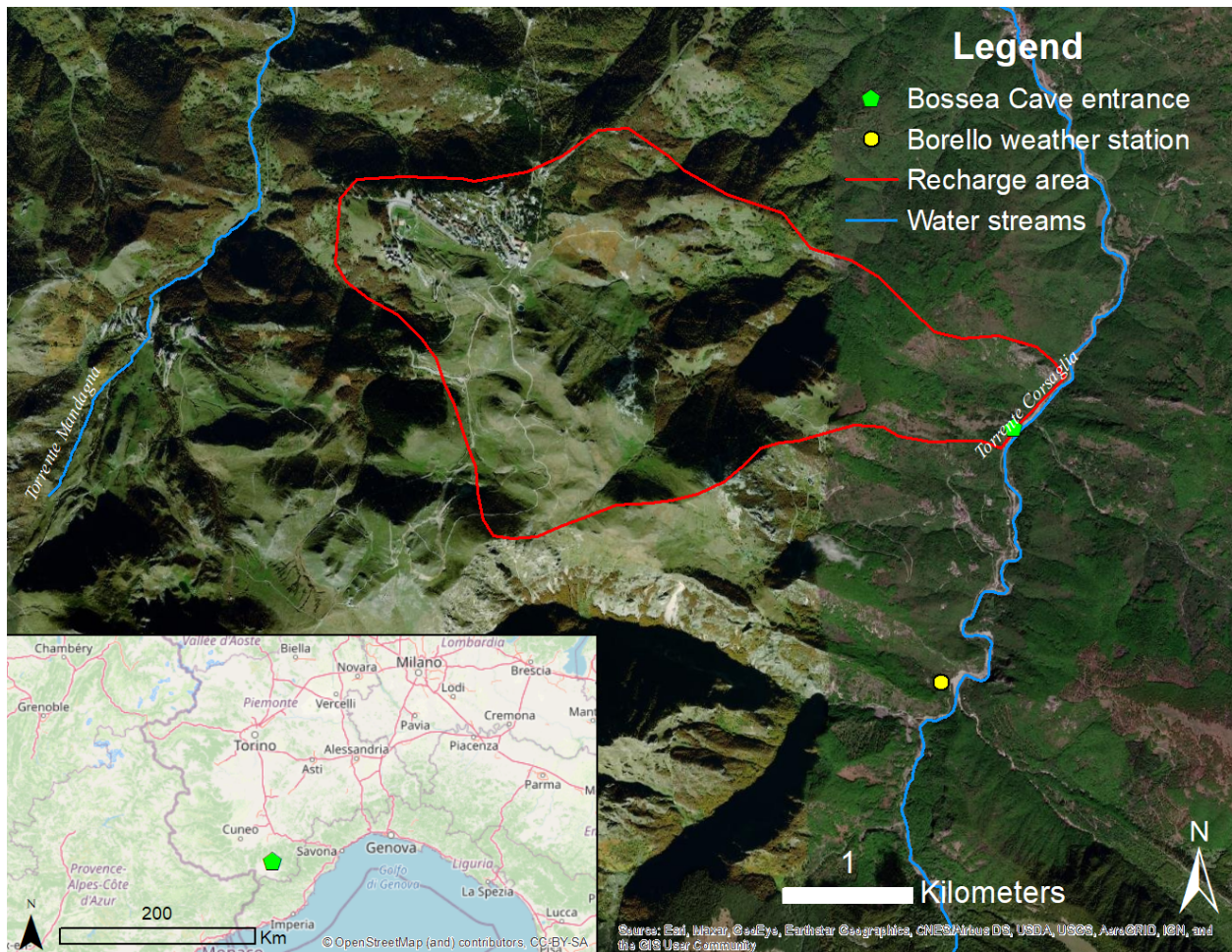


**Figure 3.** Map of the study area. The aquifer basin, the Bossea cave entrance, and the Borello weather station are shown. The flow rates are measured inside the Bossea cave close to the entrance, and the weather data, at the Borello station.

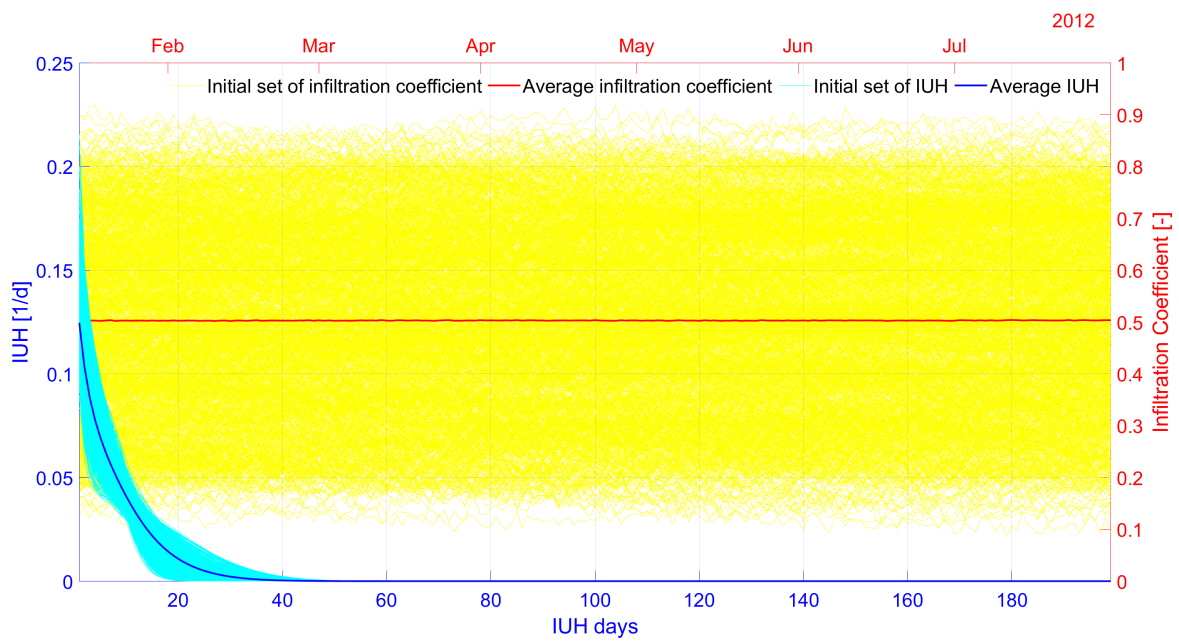


**Figure 4.** Initial ensembles of IUHs and infiltration coefficients.

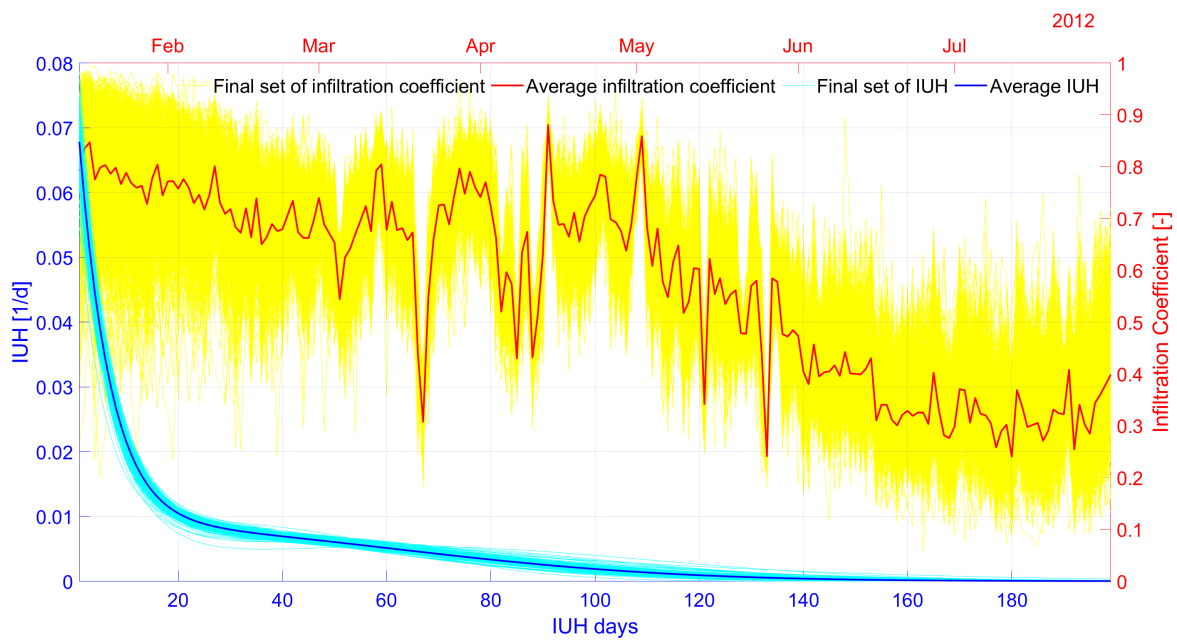


**Figure 5.** Final IUHs and infiltration coefficients. In light blue the ensemble of 1000 final IUHs, with its mean in dark blue. In yellow the ensemble of infiltration coefficient curves, with its mean in red.

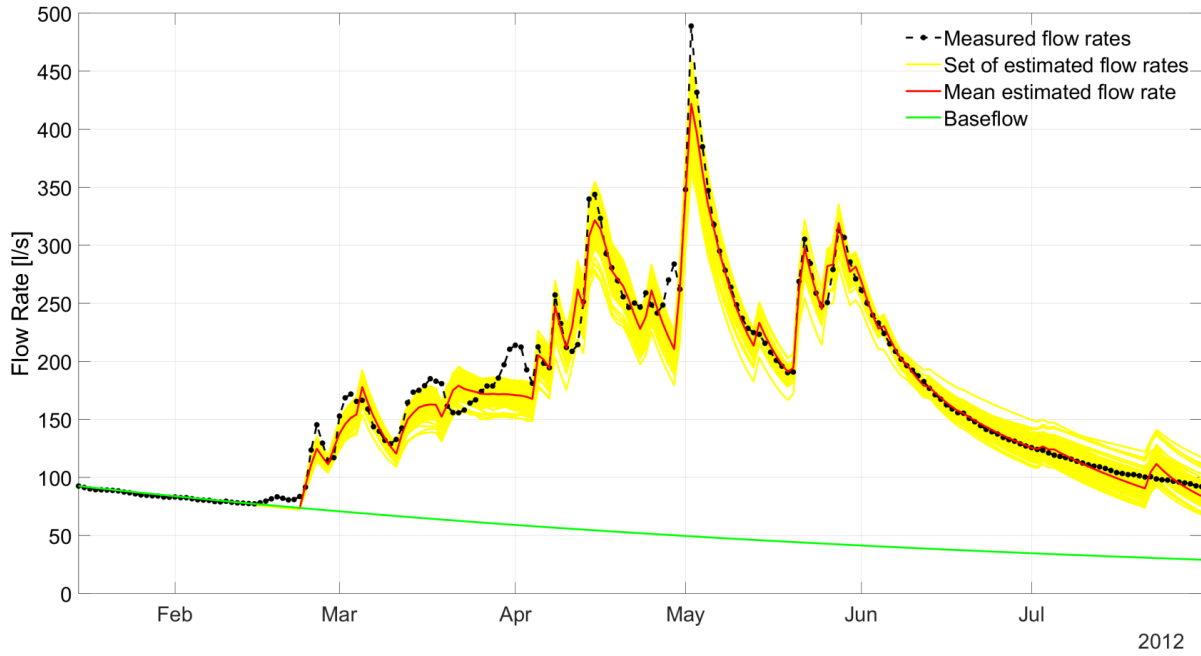
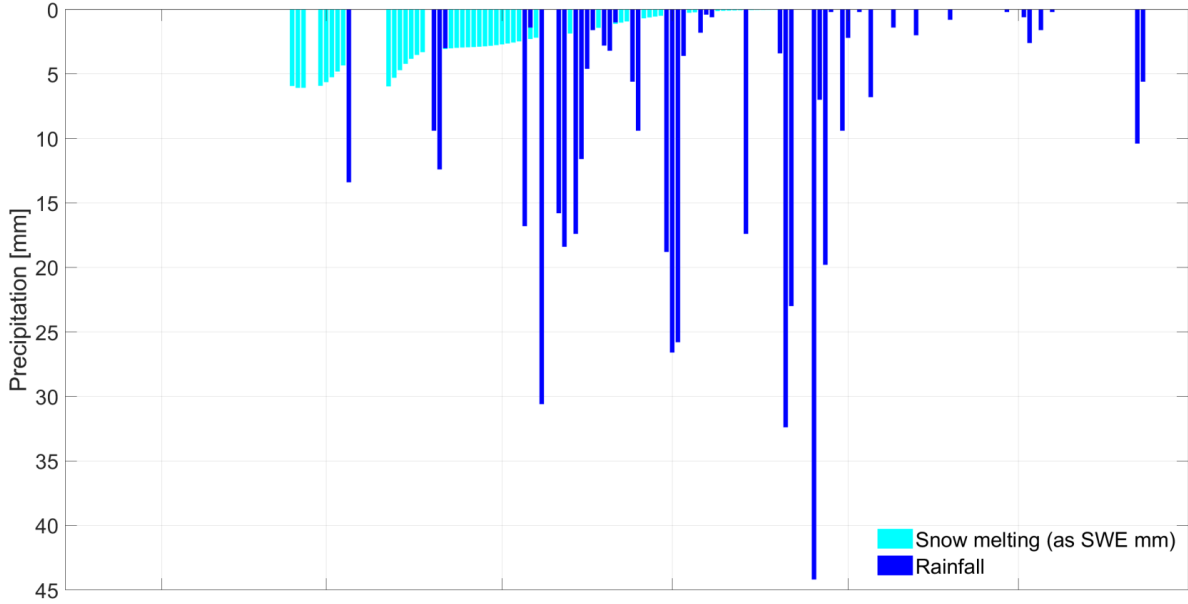


**Figure 6.** Predicted discharges. In yellow, the predictions with the 1000 members of the final ensemble of parameters, and in red, the average of these predictions. Also shown, the base flow computed with the median of the ensemble base flow parameters, and the snow water equivalent computed with the median of the parameters of the water equivalent model.

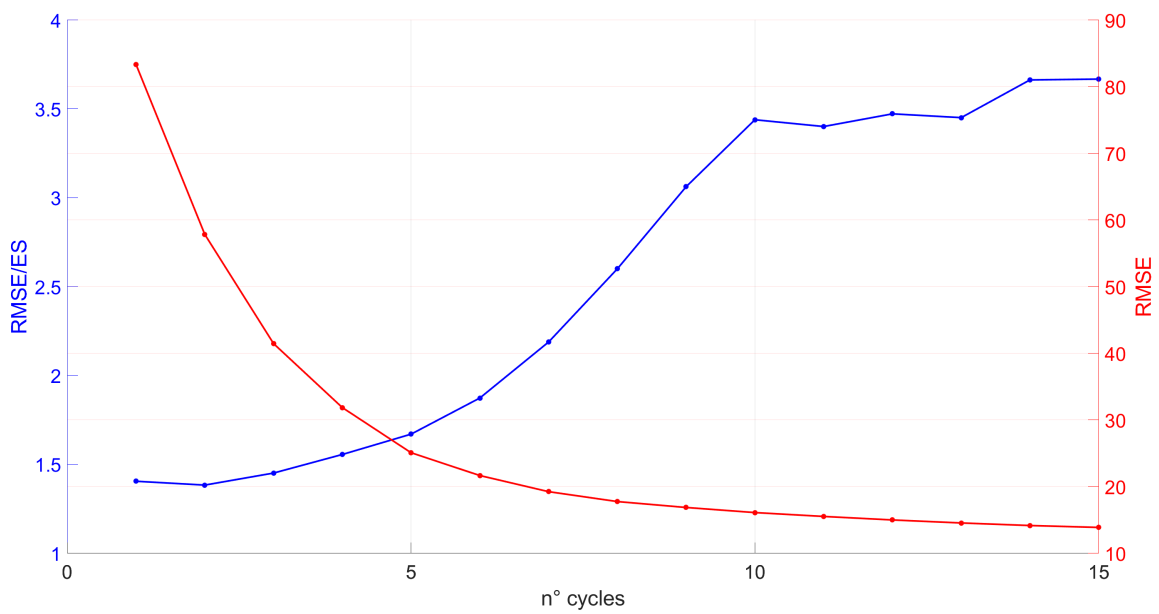


**Figure 7.** Evolution with the number of data assimilation cycles of the Root Mean Square Error (RMSE) and the ratio RMSE to Ensemble Spread (ES).

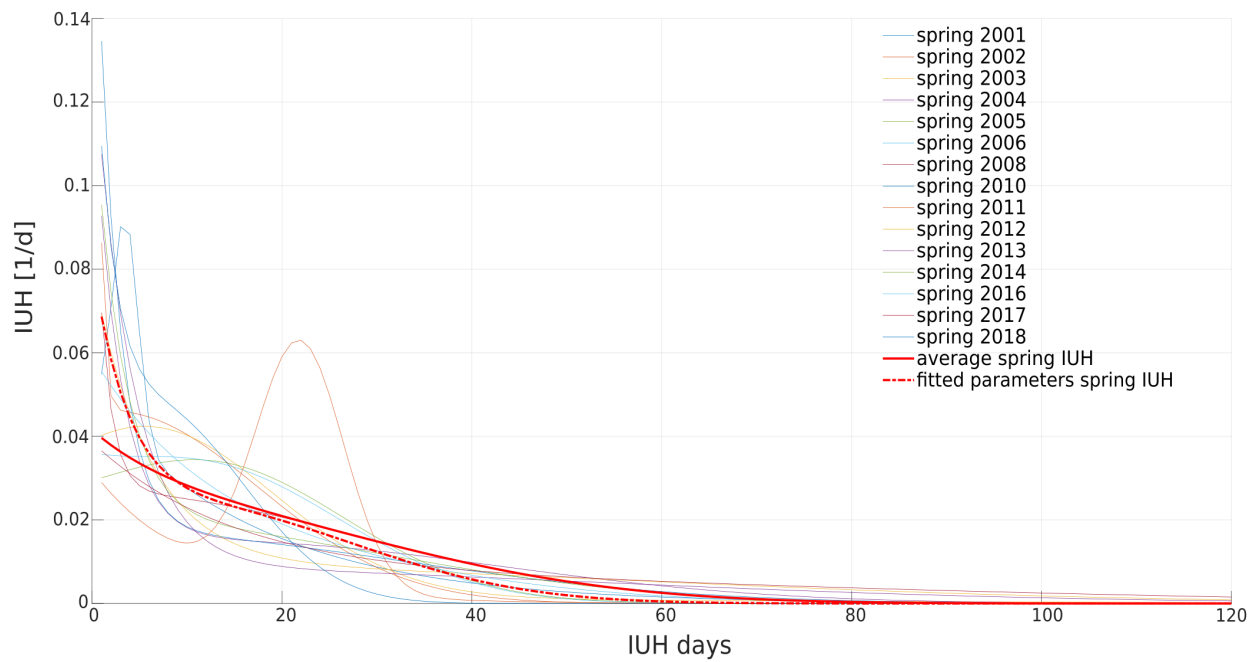


**Figure 8.** The mean of the IUHs obtained for all the spring events and the two alternative average values: in solid red, the IUH computed with the average parameters, and in dashed red, the parametric curve fitted to the average of the event IUHs.

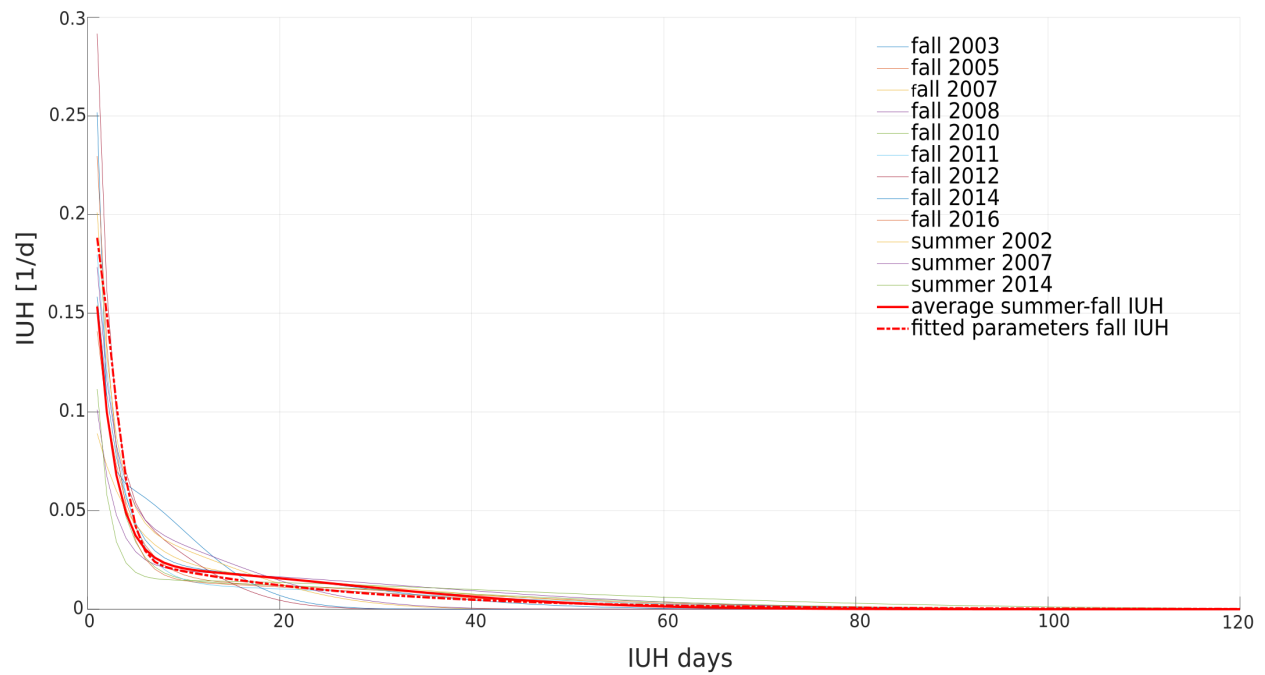


**Figure 9.** Mean of the IUHs obtained for all the summer/fall events and the two alternative average values: in solid red, the IUH computed with the average parameters, and in dashed red, the parametric curve fitted to the average of the event IUHs.

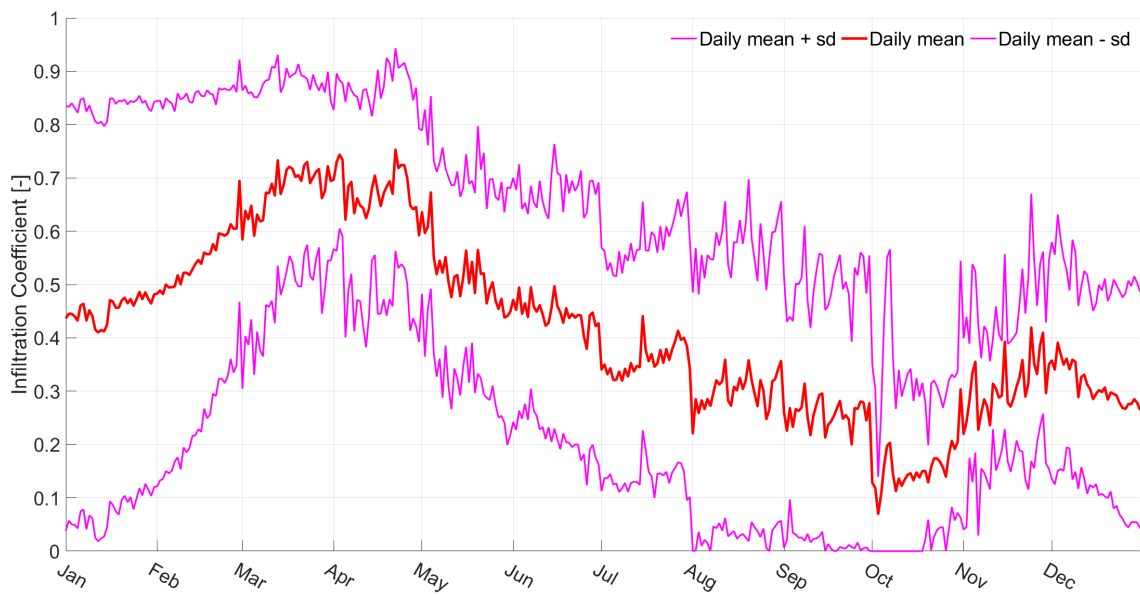


**Figure 10.** Daily infiltration coefficients. In red, the average value of the coefficients computed over all events, and in blue the uncertainty band of one-standard deviation width.

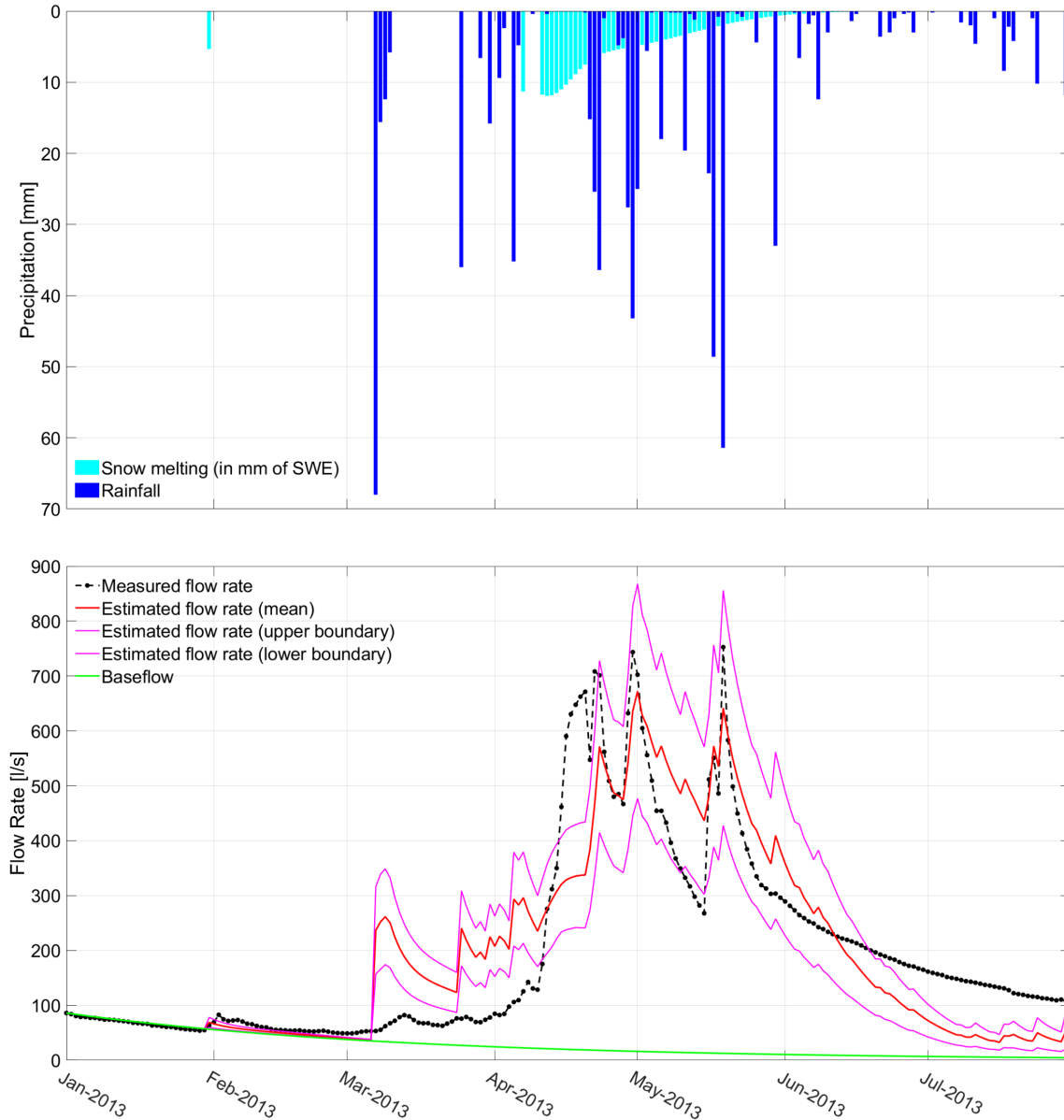


**Figure 11.** Blind forecast of the spring 2013 event. The black dotted line is the observed discharge, the solid red line is the prediction with the average model, and the two purple lines are the predictions using the infiltration coefficients in the band's limits shown in Fig. 10. For completeness, rain and snow equivalent infiltration, and base flow are also shown.

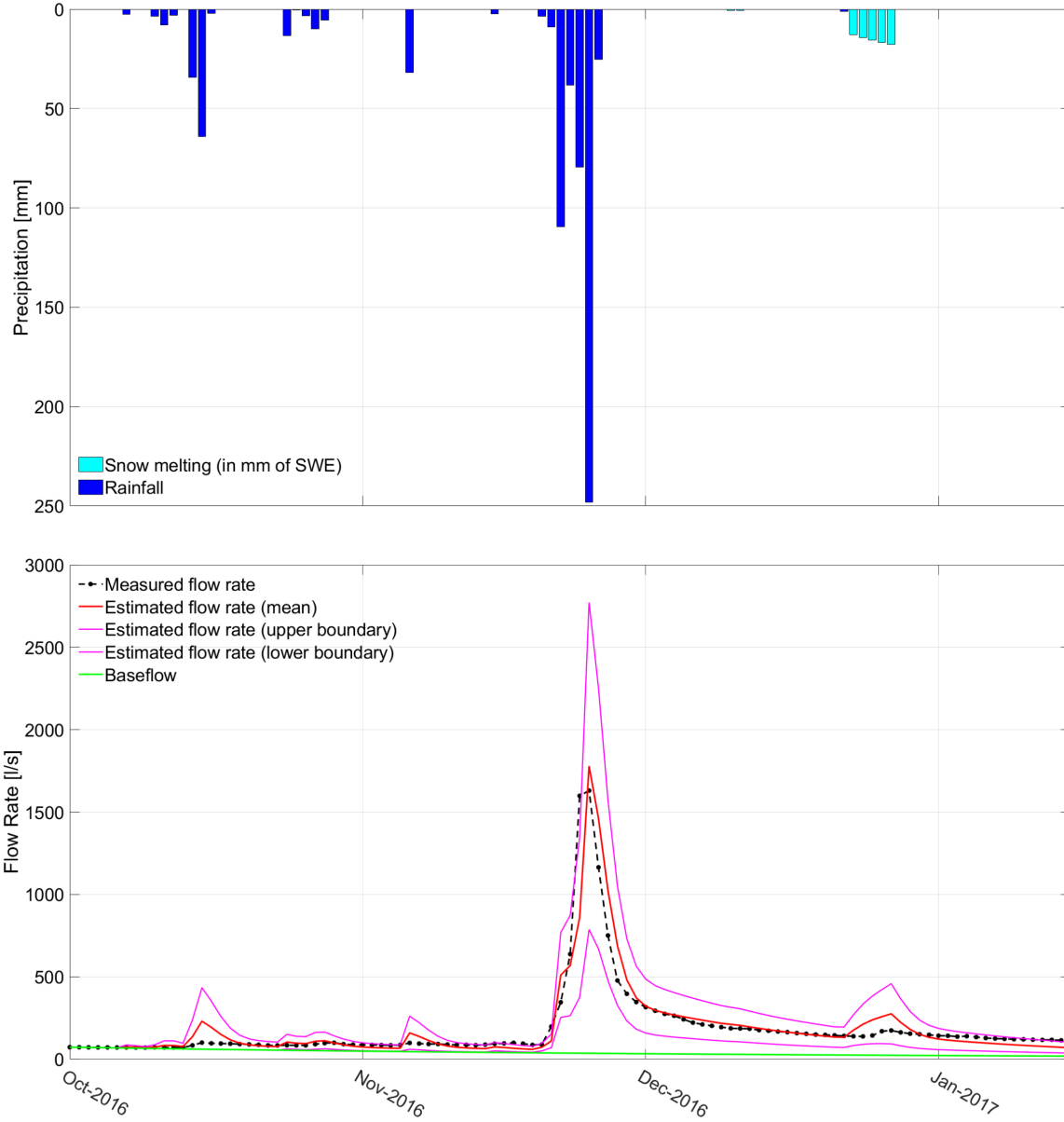


**Figure 12.** Blind forecast of the fall 2016 event. The black dotted line is the observed discharge, the solid red line is the prediction with the average model, and the two purple lines are the predictions using the infiltration coefficients in the band’s limits shown in Fig. 10. For completeness, rain and snow equivalent infiltration, and base flow are also shown.